

PAPER • OPEN ACCESS

Atomic configuration controlled photocurrent in van der Waals homostructures

To cite this article: Ying Xiong *et al* 2021 *2D Mater.* **8** 035008

View the [article online](#) for updates and enhancements.



PAPER

Atomic configuration controlled photocurrent in van der Waals homostructures

OPEN ACCESS

RECEIVED

21 December 2020

REVISED

31 January 2021

ACCEPTED FOR PUBLICATION

17 February 2021

PUBLISHED

24 March 2021

Original Content from this work may be used under the terms of the [Creative Commons Attribution 4.0 licence](#).

Any further distribution of this work must maintain attribution to the author(s) and the title of the work, journal citation and DOI.

Ying Xiong¹, Li-kun Shi^{1,2} and Justin C W Song^{1,*} ¹ Division of Physics and Applied Physics, Nanyang Technological University, 637371, Singapore² Max Planck Institute for the Physics of Complex Systems, 01187 Dresden, Germany

* Author to whom any correspondence should be addressed.

E-mail: justinsong@ntu.edu.sg**Keywords:** topological materials, bulk photovoltaic effect, non-linear optics, opto-electronic, photocurrent, strainSupplementary material for this article is available [online](#)**Abstract**

Conventional photocurrents at a p–n junction depend on macroscopic built-in fields and are typically insensitive to the microscopic details of a crystal's atomic configuration. Here we demonstrate how atomic configuration can control photocurrent in van der Waals (vdW) materials. In particular, we find bulk shift photocurrents (SPCs) can display a rich (atomic) configuration dependent phenomenology that range from contrasting SPC currents for different stacking arrangements in a vdW homostructure (e.g. AB vs BA stacking) to a strong light polarization dependence for SPC that align with crystallographic axes. Strikingly, we find that SPC in vdW homostructures can be directed by modest strain, yielding sizeable photocurrent magnitudes under unpolarized light irradiation and manifesting even in the absence of p–n junctions. These demonstrate that SPC are intimately linked to how the Bloch wavefunctions are embedded in real space, and enables a new macroscopic transport probe (photocurrent) of lattice-scale registration in vdW materials.

The atomic scale registration formed when two van der Waals (vdW) layers are stacked on top of each other can have a profound influence on its electronic behaviour [1, 2]. Prime examples include strongly correlated phases in moiré superlattices [3–5], constructing topologically non-trivial bands from topologically trivial materials through stacking [6, 7], as well as new types of collective modes (e.g. moiré excitons in twisted transition metal dichalcogenides (TMDs) [8–11]). Yet in many instances, identifying the stacking arrangement can be challenging since multiple stacking configurations can yield the same electronic energy dispersion, for e.g. AB and BA stacking alignments in vdW bilayers possess the same energy dispersion (figure 1), but contrasting atomic registrations and Bloch wavefunctions.

Here we show that photocurrents excited in vdW homostructures can be highly sensitive to its stacking and local atomic configuration. To demonstrate this, we focus on shift photocurrents (SPCs) that can be induced in the *absence* of p–n junctions [12–17] in inversion symmetry broken vdW materials [18]. In particular, we find that SPC in vdW homostructures can be directly controlled by the local

atomic configuration: for example, we find that in bilayer graphene (BLG), SPC flows in opposite directions for AB vs BA stacking (figure 1), exhibits a strong light-polarization dependence flowing transverse (longitudinal) when polarization is aligned perpendicular (parallel) to a mirror axis (figure 2), and can be directed by a local strain profile (figure 3) yielding sizeable currents even for unpolarized light and modest strain values. While we concentrate on BLG as an illustrative example, as we argue below, atomic configuration sensitivity extends to a host of other vdW materials.

The sensitivity SPC displays to local atomic configuration contrasts starkly with that of conventional p–n junction photocurrents (e.g. photovoltaic, photothermoelectric or bolometric effects) that arise in the presence of a built-in field or a bias field [19–25]. The direction (i.e. sign) of these conventional photocurrents only depends on macroscopic and slowly varying variables, such as a built-in field or Seebeck coefficient; as such these conventional photocurrents display photocurrent sign that is insensitive to registration or band gap sign [19–25]. In contrast, SPC in gapped BLG displays a sign that

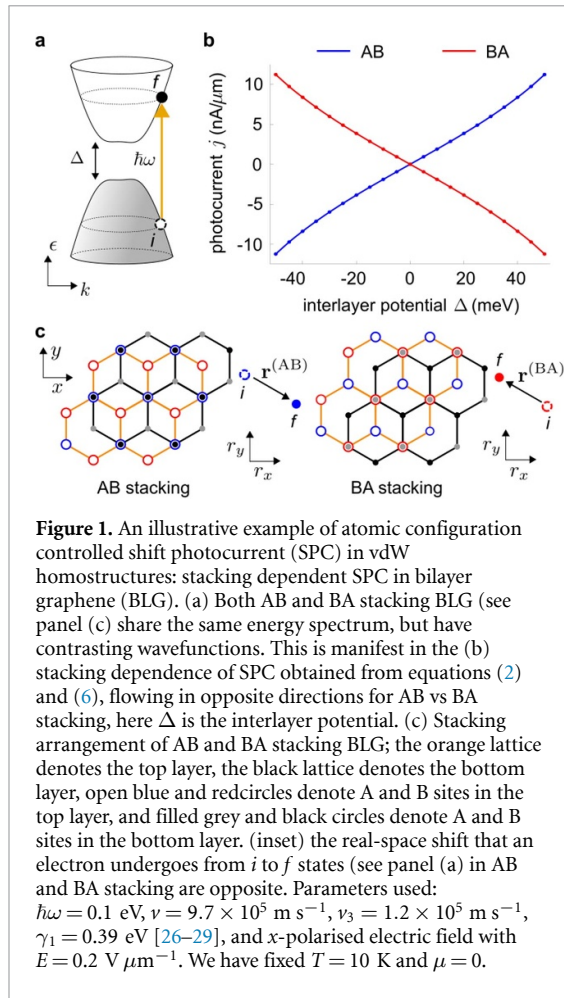


Figure 1. An illustrative example of atomic configuration controlled shift photocurrent (SPC) in vdW homostructures: stacking dependent SPC in bilayer graphene (BLG). (a) Both AB and BA stacking BLG (see panel (c)) share the same energy spectrum, but have contrasting wavefunctions. This is manifest in the (b) stacking dependence of SPC obtained from equations (2) and (6), flowing in opposite directions for AB vs BA stacking, here Δ is the interlayer potential. (c) Stacking arrangement of AB and BA stacking BLG; the orange lattice denotes the top layer, the black lattice denotes the bottom layer, open blue and red circles denote A and B sites in the top layer, and filled grey and black circles denote A and B sites in the bottom layer. (inset) the real-space shift that an electron undergoes from i to f states (see panel (a)) in AB and BA stacking are opposite. Parameters used: $\hbar\omega = 0.1$ eV, $v = 9.7 \times 10^5$ m s $^{-1}$, $v_3 = 1.2 \times 10^5$ m s $^{-1}$, $\gamma_1 = 0.39$ eV [26–29], and x -polarised electric field with $E = 0.2$ V μm^{-1} . We have fixed $T = 10$ K and $\mu = 0$.

changes with registration and gap (figure 1(b)) and can be tuned by polarization (figure 2), providing a simple and readily accessible experimental signature. Indeed, as we explain below, SPC's sensitivity to atomic configuration proceeds directly from the photoexcitation process: when an electron is photoexcited (figures 1(a) and (c)), it undergoes a real-space displacement, $\mathbf{r}_{i \rightarrow f}$, that depends on how the Bloch wavefunctions are embedded in real space as encoded in its atomic configuration. This renders SPC a sensitive diagnostic of the atomic registration of vdW homostructures.

We expect atomic configuration sensitive SPC can be readily found in currently available vdW homobilayers (e.g. gapped BLG) and other homostructures. For instance, stacking dependence can be probed across stacking faults [30]; polarization dependence of SPC can be used to identify crystallographic axes. We note that stacking dependent SPC is particularly pronounced in gapped BLG due to its strong interlayer hybridization [31, 32] that distinguish the wavefunctions from different stacking configurations (e.g. AB/BA). This stands in contrast to vdW heterobilayers (e.g. MoSe $_2$ /WSe $_2$) where interlayer hybridization can be weak [33–38], producing a bandstructure and electronic wavefunctions that are dominated by other factors, such as their type II band

alignment [33–38]. As a result, in what follows, we will focus on vdW homostructures, and gapped BLG in particular where interlayer coupling is strong, to exemplify the atomic configuration SPC.

Shift vector and SPC—We begin by examining the form of SPC that arises from the real space displacement $\mathbf{r}_{v \rightarrow c}$ that an electron undergoes as it is photoexcited from the valence (v) to conduction (c) band [12–14, 39]: $\mathbf{j} = e \sum_{v \rightarrow c} W_{v \rightarrow c} \mathbf{r}_{v \rightarrow c}$, where $W_{v \rightarrow c}$ is the rate of photo-excitation from the v to c bands. For vertical transitions, this displacement is described by a shift vector that depends on the electronic wavefunction in c, v bands [14, 39]:

$$\mathbf{r}(\theta, \mathbf{k}) = \mathbf{A}_c(\mathbf{k}) - \mathbf{A}_v(\mathbf{k}) - \nabla_{\{\mathbf{k}\}} \arg[\nu_\theta(\mathbf{k})], \quad (1)$$

where \mathbf{k} is the wavevector of the electron, $\mathbf{A}_{c(v)}(\mathbf{k}) = i \langle u_{c(v)}(\mathbf{k}) | \nabla_{\{\mathbf{k}\}} | u_{c(v)}(\mathbf{k}) \rangle$ is the Berry connection of the conduction (valence) band, $\nu_\theta(\mathbf{k}) = \langle u_c(\mathbf{k}) | \hat{\mathbf{e}}_\theta \cdot \hat{v} | u_v(\mathbf{k}) \rangle$ is the velocity matrix element with $\hat{v} = \partial_{\{\mathbf{k}\}} H(\mathbf{k}) / \hbar$ the velocity operator, $u_{c(v)}(\mathbf{k})$ is the Bloch wavefunction and $\hat{\mathbf{e}}_\theta$ is the incident light electric field polarisation oriented θ away from x -axis. $H(\mathbf{k})$ is the Bloch hamiltonian; here we use \mathbf{k} measured away from the Γ point.

Using equation (1), SPC can be written as [14, 39]

$$\mathbf{j} = C \int d^2 \mathbf{k} \rho(\mathbf{k}) \mathbf{R}(\theta, \mathbf{k}), \quad \mathbf{R}(\theta, \mathbf{k}) = |\nu_\theta|^2 \mathbf{r}(\theta, \mathbf{k}), \quad (2)$$

where $C = (e/8\pi)(eE/\hbar\omega)^2$, E is the amplitude of the electric field strength of the incident light, ω is the light frequency. The factor $\rho(\mathbf{k}) = (f(\epsilon_{v\mathbf{k}}) - f(\epsilon_{c\mathbf{k}}))\delta(\omega_{cv} - \omega)$ defines the iso-energy contour that satisfies energy conservation, and $f(\epsilon_{c(v)\mathbf{k}})$ is the Fermi–Dirac distribution of electrons.

SPC in equation (2) is particularly sensitive to the symmetries of the electronic system manifest in the shift vector. For instance, in the presence of inversion symmetry, the shift vector $\mathbf{r}(\theta, \mathbf{k}) = -\mathbf{r}(\theta, -\mathbf{k})$ is odd. As a result, when there is inversion symmetry, equation (2) vanishes [39]; breaking inversion symmetry is required for a finite shift current.

Symmetry, configuration, and stacking dependence—As we now explain, the shift vector is highly sensitive to the atomic configuration. In so doing, we concentrate on stacked bilayers, and introduce a stacking index $\eta = \{\text{AB}, \text{BA}\}$ to describe the stacking configuration (e.g. found in BLG) as well as an interlayer potential difference Δ between top and bottom layers. For concreteness and clarity of presentation, in the main text we will concentrate on BLG where the electronic excitations can be treated as effectively spinless particles. We emphasize that our conclusions and analysis applies more broadly to other vdW materials and homostructures such as monolayer TMDs, bilayer 2 H TMDs, as well as gapped graphene on hexagonal Boron Nitride (G/hBN), see discussion

in supplementary information (SI) (available online at stacks.iop.org/2DM/8/035008/mmedia) [40].

We proceed by analyzing the crystalline symmetries of Bernal stacked gapped BLG [31, 41–43]: they possess a three-fold in-plane rotation C_3^z symmetry and mirror symmetry (MS) about axes that connect the non-dimer sites (figure 1(c)). For example, MS about the y -axis demands $\mathcal{M}_y H^{(\eta)}(\Delta, \mathbf{k}) \mathcal{M}_y^{-1} = H^{(\eta)}(\Delta, \mathcal{M}_y \mathbf{k})$; here \mathcal{M}_y is the mirror operation about the y -axis [i.e. $(x, y) \rightarrow (-x, y)$]. Applying MS as well as time-reversal symmetry [44], we find that $\mathbf{r}^{(\eta)}(\Delta, \theta, \mathbf{k})$ transforms as

$$\begin{aligned} r_x^{(\eta)}(\Delta, \theta, k_x, k_y) &= -r_x^{(\eta)}(\Delta, -\theta, k_x, -k_y), \\ r_y^{(\eta)}(\Delta, \theta, k_x, k_y) &= r_y^{(\eta)}(\Delta, -\theta, k_x, -k_y). \end{aligned} \quad (3)$$

In obtaining equation (3), we noted that $\mathbf{r}^{(\eta)}(\Delta, \theta, \mathbf{k}) = \mathbf{r}^{(\eta)}(\Delta, \theta + \pi, \mathbf{k})$ since light polarisations along $\hat{\mathbf{e}}_\theta$ and $-\hat{\mathbf{e}}_\theta$ are equivalent. While we have focussed on MS about the y -axis in equation (3), there are two other mirror axes related to \mathcal{M}_y via C_3^z rotation from the y -axis. In a similar fashion, mirror reflection about these directions produce the same shift vector symmetry relations (for parallel and perpendicular components) as equation (3), see SI [40].

Interestingly, when the light polarization $\hat{\mathbf{e}}_\theta$ is directed parallel (perpendicular) to a mirror axis, e.g. $\theta = \pi/2$ ($\theta = 0$), the shift vector (see equation (3)) acts as pseudovector; r_x flips sign whereas r_y remains constant as $k_y \rightarrow -k_y$. As we will see below, this severely constrains the direction of SPC. For example, when $\hat{\mathbf{e}}_\theta$ is parallel to a mirror axis (e.g. $\theta = \pi/2$), SPC is purely longitudinal, flowing parallel to the polarization of light. Similarly, when $\hat{\mathbf{e}}_\theta$ is perpendicular to a mirror plane (e.g. $\theta = 0$), SPC is purely *transverse* (perpendicular to $\hat{\mathbf{e}}_\theta$). This latter SPC flow is particularly striking since SPC flows transverse to the incident ac (light) electric field, underscoring the geometric origin of the SPC.

We now move to the symmetry constraints relating the stacking configurations. AB and BA stackings are related by flipping the sample about the y -axis (figure 1(c)). For example, the real space Hamiltonians of AB and BA stacked bilayer graphene are related by a π rotation about the y -axis: $C_2^y \mathcal{H}^{(\text{AB})}(\Delta, \mathbf{r}) (C_2^y)^{-1} = \mathcal{H}^{(\text{BA})}(-\Delta, \mathbf{r})$ where $C_2^y: (x, y, z) \rightarrow (-x, y, -z)$ is the rotation operation. As a result, the Bloch Hamiltonian obeys the symmetry constraint $C_2^y H^{(\text{AB})}(\Delta, \mathbf{k}) (C_2^y)^{-1} = H^{(\text{BA})}(-\Delta, C_2^y \mathbf{k})$ (see SI [40] for detailed explanation). Using these and equation (1) we find that AB and BA stackings obey the relation:

$$\begin{aligned} r_x^{(\text{AB})}(\Delta, \theta, \mathbf{k}) &= -r_x^{(\text{BA})}(-\Delta, -\theta, C_2^y \mathbf{k}), \\ r_y^{(\text{AB})}(\Delta, \theta, \mathbf{k}) &= r_y^{(\text{BA})}(-\Delta, -\theta, C_2^y \mathbf{k}). \end{aligned} \quad (4)$$

In obtaining equation (4) we have used that the x component of the velocity matrix element switches

sign under C_2^y [i.e. $\hat{v}_x \rightarrow -\hat{v}_x$]; this is equivalent to mapping $\theta \rightarrow \pi - \theta$.

Noting that under an inversion operation, the shift vector transforms as $\mathbf{r}^{(\eta)}(\Delta, \theta, \mathbf{k}) = -\mathbf{r}^{(\eta)}(-\Delta, \theta, -\mathbf{k})$ [40], and applying equation (3) onto equation (4) we obtain AB/BA stacking dependent shift vectors that have opposite signs:

$$\mathbf{r}^{(\text{AB})}(\Delta, \theta, \mathbf{k}) = -\mathbf{r}^{(\text{BA})}(\Delta, \theta, \mathbf{k}). \quad (5)$$

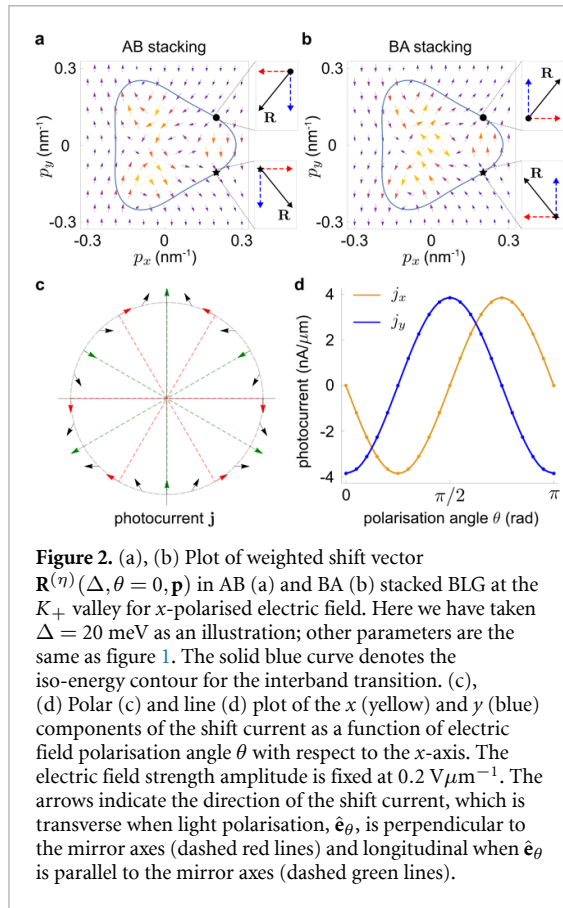
In obtaining equation (5), we noted $C_2^y: (k_x, k_y) \rightarrow (-k_x, k_y)$, and applied the time-reversal operation. We remark that this stacking dependence can be understood physically from the inversion-symmetry breaking in the unit cell. For a fixed interlayer potential difference, a change in the stacking order from AB to BA switches the directionality of the in-plane dipole between the non-dimer site, as illustrated in figure 1(c). Similarly, when interlayer potential is flipped (keeping stacking order the same), the in-plane dipole similarly changes sign. Since the shift vector is sensitive to the electric dipole configuration, this leads to a stacking dependent shift vector in equation (5). As we will see below, this directly produces the sign flip of SPC shown in figure 1(b).

Illustration: gapped BLG—We now turn to exemplify the stacking (and configuration) dependent SPC in a minimal model of an AB/BA stacked material: BLG. Bernal stacked BLG can be described by a four-band minimal model in the basis $\{\psi_{A_t}, \psi_{B_t}, \psi_{A_b}, \psi_{B_b}\}$, where $A_{t,b}, B_{t,b}$ stand for A and B sites on the top and bottom layers respectively. The Hamiltonian for AB/BA stacked BLG [31, 45] can be described via $H^{(\eta)} = H_0^{(\eta)} + H_w^{(\eta)}$, where $H_0^{(\eta)}$ and $H_w^{(\eta)}$ read

$$\begin{aligned} H_0^{(\eta)} &= \hbar v (\xi p_x \sigma_x + p_y \sigma_y) \tau_0 + \frac{\Delta}{2} \sigma_0 \tau_z + \frac{\gamma_1}{2} \\ &\quad \times (\sigma_x \tau_x + \eta \sigma_y \tau_y), \\ H_w^{(\eta)} &= \frac{\hbar v_3}{2} [\xi p_x (\sigma_x \tau_x - \eta \sigma_y \tau_y) - p_y (\sigma_y \tau_x + \eta \sigma_x \tau_y)] \end{aligned} \quad (6)$$

where $\mathbf{p} = \mathbf{k} - \mathbf{K}_\xi$ is the wavevector measured from \mathbf{K}_ξ with $\xi = \pm$ denoting the two valleys. The Pauli matrices σ and τ label the sublattice and layer degrees of freedom respectively, and $\eta = \pm$ for AB and BA stacking configurations. Here v is the Fermi velocity in each layer, and γ_1 is the direct interlayer hopping. The term H_w provides a trigonal warping effect of the energy dispersion with v_3 describing the interlayer hopping between the nondimer site [31, 45]. An interlayer potential difference Δ opens a gap in the system and breaks inversion symmetry.

Even though trigonal warping v_3 is typically an order of magnitude smaller than v [26–29], it is nevertheless responsible for enforcing the three-fold symmetry of the bilayers. Importantly, trigonal warping $H_w^{(\eta)}$ is necessary to achieve a non-zero shift current. This can be seen by noting that in the absence



of trigonal warping, the low energy dispersion in each valley exhibits an emergent $U(1)$ continuous rotational symmetry. For any linear polarisation $\hat{\mathbf{e}}_\theta$, reflection symmetries about axes both parallel and perpendicular to $\hat{\mathbf{e}}_\theta$ yield a vanishing shift current.

Numerically computing the shift vector in equation (1) using the eigensolutions of equation (6) we obtain the stacking dependent (weighted shift vector) $\mathbf{R}^{(n)}(\Delta, \theta, \mathbf{p}) = \mathbf{r}^{(n)}(\Delta, \theta, \mathbf{p}) |\nu_\theta^{(n)}(\mathbf{p})|^2$ in figures 2(a) and (b). We note that $|\nu_\theta^{(n)}(\mathbf{p})|^2$ and $\rho(\mathbf{p})$ in equation (2) depend only on energy dispersion and are independent of stacking or the gap sign. Here we have chosen an x -polarized electric field, $\theta = 0$ as an illustration, see SI for other polarizations. As expected from equation (5), $\mathbf{R}^{(n)}$ in figures 2(a) and (b) flips sign when stacking arrangement changes from AB to BA even when the same interlayer potential is applied. As a result, SPC also switches sign when the shift vector flips sign. Numerically integrating equation (2) with the weighted shift vector in figures 2(a) and (b) over both valleys (and spins) for a chemical potential in the middle of the gap and $T = 10$ K, we obtain a stacking dependent SPC shown in figure 1(b), that flips sign when either stacking arrangement is changed (AB \rightarrow BA) or interlayer potential is switched ($\Delta \rightarrow -\Delta$).

We note that the magnitude of SPC increases as $|\Delta|$ increases yielding sizeable photocurrents of order several $\text{nA } \mu\text{m}^{-1}$ in figure 1(b) for modest

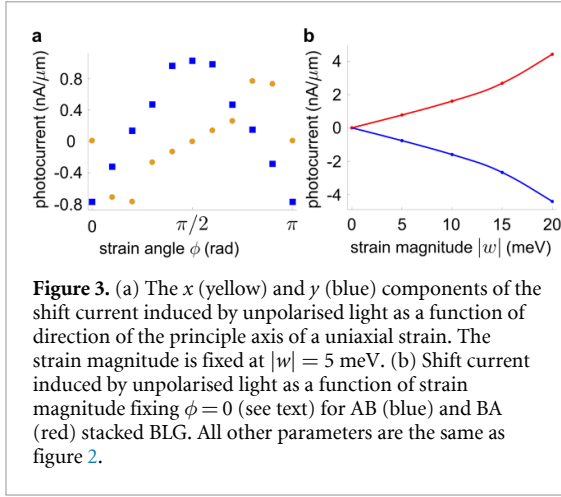
light irradiation (see parameters in caption); it vanishes when no interband transitions occur. While we find maximal SPC occur when chemical potential is in the gap (shown in figure 1(b)), sizeable SPC can still manifest when BLG is doped, but diminish when $2E_F \sim \hbar\omega$ due to Pauli blocking.

As discussed above in equation (3), the shift vector can exhibit a pseudovector nature. This is displayed in figures 2(a) and (b) for $\theta = 0$, wherein recalling that $|\nu_\theta^{(n)}(\mathbf{p})|^2$ is even, we have $R_x \rightarrow -R_x$ as $p_y \rightarrow -p_y$ whereas R_y remains unchanged, see e.g. weighted shift vector on solid circle vs star positions in figures 2(a) and (b) inset. Here we have noted that by mapping $k_y \rightarrow -k_y$ (measured from Γ), $p_y \rightarrow -p_y$ in the same valley (see SI).

This pseudovector nature (shown in figures 2(a) and (b)) yields SPC for $\theta = 0$ in equation (2) that is purely in the y -direction—transverse to $\hat{\mathbf{e}}_{\theta=0}$. This is manifested in figure 2(c), where we plot the SPC \mathbf{j} as a function of polarization angle θ where the dashed lines denote magnitude of SPC and the arrows denote its direction. Strikingly, along polarizations perpendicular to a mirror axes ($\theta = 0, \pm 2\pi/3$, red dashed lines), the shift current is purely transverse (red arrows) to the polarization. This underscores the geometrical origin of SPC with a current that is perpendicular to the applied (oscillating) electric field. In contrast, when light polarization is applied *parallel* to a mirror axes ($\theta = \pi/2, \pm\pi/6$), SPC is purely longitudinal (green arrows). As a result, SPC alignment with the crystal axes and its polarization dependence (figure 2(d)) can be used to determine a vdW device's crystallographic orientation.

Strain photocurrent in vdW stacks—While large stacking and configuration dependent SPC manifest in the presence of polarized light (discussed above), due to the C_3^z symmetry of the Bernal stacked bilayers, photocurrent vanishes for *unpolarized* light irradiation; for a detailed discussion, see SI [40]. However, when an in-plane strain is applied, it breaks the C_3^z symmetry of the Bernal stacked bilayers, and as we now discuss, enables a strain induced SPC even for unpolarized light. We note that 2D materials can accommodate strains from several to ~ 10 percent [46–49]; in addition to extrinsically applied strains [46–49], strain profiles can also be naturally found in many moire material stacks [50]. We note that strain has recently emerged as a tool for controlling bulk photocurrents [51–56].

To illustrate such a strain-induced photocurrent in BLG, we consider a uniaxial strain applied in BLG that can be described by $\tilde{H}^{(n)} = \tilde{H}_0^{(n)} + \tilde{H}_w^{(n)} + H_s^{(n)}$ [57, 58], where $\tilde{H}_0^{(n)}$ and $\tilde{H}_w^{(n)}$ can be obtained from equation (6) but replacing \mathbf{p} to $\tilde{\mathbf{p}} = \mathbf{p} + \mathbf{A}_0/v$. Here $\mathbf{A}_0 = A_0(\cos 2\phi, -\xi \sin 2\phi)$ describes a shift of the valleys in k -space, where ϕ is the angle of the strain principle axis with respect to the x -axis. The additional terms $H_s^{(n)}$



describes the modification of the skew interlayer coupling by the strain and is given by [57, 58] $H_s^{(\eta)} = [w_x(\sigma_x\tau_x - \eta\sigma_y\tau_y) - w_y(\sigma_y\tau_x + \eta\sigma_x\tau_y)]/2$, where $\mathbf{w} = |w|(\cos 2\phi, -\xi \sin 2\phi)$ accounts for both the (in-plane) uniaxial strain and an interlayer shear associated with it [57, 58]. In BLG, 2% of strain corresponds to $|w| \approx 19$ meV [57, 58]. We note that the shift of the valleys does not affect the shift current since it involves integration over the entire k -space. In the following, we will focus on the effect of \mathbf{w} .

When BLG is strained, we find that the shift currents at different polarisation angles do not cancel out. Instead, a net shift current (upon integration over all polarisations) manifests—the strain photocurrent: $\mathbf{J}^{\text{tot}} = \int \mathbf{j}(\theta)d\theta$. Strain photocurrents are shown in figures 3(a) and (b) where we have numerically integrated equation (2) together with the eigensolutions of strained BLG above. As expected, strain photocurrents increase with increasing strain (figure 3(b)), achieving sizeable values of order $\text{nA } \mu\text{m}^{-1}$ for modest strain values and incident light irradiation (see parameters in caption). We note that, similar to that discussed for SPC, the strain photocurrent in figure 3(b) have opposite signs for AB vs BA (blue vs red).

Strain photocurrents are very sensitive to the principle axis (ϕ) of applied strain and exhibit a π periodicity, see figure 3(a). Strikingly, when strain principle axis is perpendicular (parallel) to the mirror axes, the strain photocurrent induced is transverse (longitudinal) to the applied strain direction, see e.g. strain photocurrents $\phi = 0$ ($\phi = \pi/2$) in figure 3(a). As we now explain, this directly proceeds from the symmetry of the bilayer stacks. We write the strain photocurrent in terms of its symmetric and antisymmetric (w.r.t. θ) contributions

$$J_i^{\text{tot}} = C \sum_{\xi=\pm} \int \int d\theta d\mathbf{p} \rho(\mathbf{p}) [V_s(\theta, \mathbf{p})(r_i(\theta, \mathbf{p}) + r_i(-\theta, \mathbf{p})) + V_a(\theta, \mathbf{p})(r_i(\theta, \mathbf{p}) - r_i(-\theta, \mathbf{p}))], \quad (7)$$

where $V_s(\theta, \mathbf{p}) = |\nu_x(\mathbf{p})|^2 \cos^2 \theta + |\nu_y(\mathbf{p})|^2 \sin^2 \theta$ is the component of $|\nu_\theta(\mathbf{p})|^2$ that is symmetric in θ , and $V_a(\theta, \mathbf{p}) = 2\Re[\nu_x(\mathbf{p})\nu_y(\mathbf{p})^*] \sin \theta \cos \theta$ is the component that is antisymmetric in θ . Here $\int d\theta$ denotes an integral of polarization angle between $0 \leq \theta \leq \pi/2$ and we have omitted mention of the stacking index η and interlayer potential difference, Δ , for brevity.

Crucially, when strain is applied either parallel or perpendicular to the mirror axes, MS about the mirror axis is preserved. These constrain the integrand of equation (7). For example, when strain is along $\phi = 0, \pi/2$, we observe that $V_{s,a}(\theta, \mathbf{p})$ is even (odd) under $p_y \rightarrow -p_y$; similarly, the shift vector transforms according to equation (3). Combining these, we find that the integrand for J_x^{tot} is odd under $p_y \rightarrow -p_y$, whereas J_y^{tot} is even. As a result, when strain is applied along $\phi = 0$ ($\phi = \pi/2$), strain photocurrent is purely transverse (longitudinal) as shown in figure 3(a). The same reasoning can be applied for strains along other high symmetry axes, see SI [40]. This demonstrates vividly how strains can be used to direct SPC.

SPC is a quantum geometric property/response that depends on how and where the wavefunctions in the unit cell are embedded in real space. The sensitivity to the real-space embedding is particularly pronounced in gapped BLG, enabling a wealth of SPC properties that include stacking and light polarization angle dependence, as well as a sensitivity to strain in the sample. We note that such sensitivity to the atomic registration often requires scanning probe or transmission electron microscopy techniques. SPC, on the other hand, can be readily extracted at global leads in a conventional scanning photocurrent experiment [59, 60] enabling a new tool for crystallographic and strain profile characterization. Indeed, a particularly urgent venue for such characterization are low twist-angle moire materials (e.g. twisted BLG with twist angle $\lesssim 1^\circ$) wherein atomic reconstruction leads to an alternating pattern of commensurate AB and BA stacking domains with sizes as large as several hundreds of nm [50, 61, 62]. In these systems, we expect local SPC induced by light irradiation concentrated in AB vs BA stacking domains will flow in opposite directions. Furthermore, real-space strain profiles may additionally warp the direction of the polarisation dependent SPC. As a result, we anticipate SPC (aided by scanning near-field optical probes [59, 60]) can enable macroscopic transport probe of the myriad atomic registrations found in twisted materials.

From a technological perspective, we note that SPC can attain magnitudes up to tens of $\text{nA } \mu\text{m}^{-1}$ (for modest irradiation of several kW cm^{-2} and $\hbar\omega = 0.1\text{eV}$), and are comparable with those typically found in graphene based photodetectors [21]. Indeed, since gap sizes can reach large values, SPC can persist to high temperatures including room temperature. Because SPC in equation (2) scales inversely with photon frequency, we anticipate responsivities

and photocurrent will be further enhanced as ω is lowered into the THz regime.

Acknowledgments

We acknowledge insightful conversations with Arpit Arora and Qiong Ma. This work was supported by the National Research Foundation (NRF), Singapore under its NRF fellowship programme Award Number NRF-NRFF2016-05, the Ministry of Education, Singapore under its MOE AcRF Tier 3 Award MOE2018-T3-1-002, and a Nanyang Technological University start-up grant (NTU-SUG).

ORCID iD

Justin C W Song  <https://orcid.org/0000-0002-5175-6970>

References

- [1] Geim A K and Grigorieva I V 2013 Van der Waals heterostructures *Nature* **499** 419–25
- [2] Song J C W and Gabor N M 2018 Electron quantum metamaterials in van der Waals heterostructures *Nat. Nanotechnol.* **13** 986–93
- [3] Cao Y et al 2018 Correlated insulator behaviour at half-filling in magic-angle graphene superlattices *Nature* **556** 80–84
- [4] Cao Y, Fatemi V, Fang S, Watanabe K, Taniguchi T, Kaxiras E and Jarillo-Herrero P 2018 Unconventional superconductivity in magic-angle graphene superlattices *Nature* **556** 43–50
- [5] Balents L, Dean C R, Efetov D K and Young A F 2020 Superconductivity and strong correlations in moiré flat bands *Nat. Phys.* **16** 725–33
- [6] Song J C W, Samutpraphoot P and Levitov L S 2015 Topological Bloch bands in graphene superlattices *Proc. Natl Acad. Sci. USA* **112** 10879–83
- [7] Tong Q, Yu H, Zhu Q, Wang Y, Xu X and Yao W 2017 Topological mosaics in moiré superlattices of van der Waals heterobilayers *Nat. Phys.* **13** 356–62
- [8] Yu H, Liu G B, Tang J, Xu X and Yao W 2017 Moiré excitons: from programmable quantum emitter arrays to spin-orbit-coupled artificial lattices *Sci. Adv.* **3** e1701696
- [9] Tran K et al 2019 Evidence for moiré excitons in van der Waals heterostructures *Nature* **567** 71–75
- [10] Jin C et al 2019 Observation of moiré excitons in WSe₂/WS₂ heterostructure superlattices *Nature* **567** 76–80
- [11] Evgeny A M et al 2019 Resonantly hybridized excitons in moiré superlattices in van der Waals heterostructures *Nature* **567** 81–86
- [12] Kraut W and von Baltz R 1979 Anomalous bulk photovoltaic effect in ferroelectrics: a quadratic response theory *Phys. Rev. B* **19** 1548–54
- [13] von Baltz R and Kraut W 1981 Theory of the bulk photovoltaic effect in pure crystals *Phys. Rev. B* **23** 5590–6
- [14] Sipe J E and Shkrebtii A I 2000 Second-order optical response in semiconductors *Phys. Rev. B* **61** 5337–52
- [15] Young S M and Rappe A M 2012 First principles calculation of the shift current photovoltaic effect in ferroelectrics *Phys. Rev. Lett.* **109** 116601
- [16] Koch W T H, Munser R, Ruppel W and Würfel P 1976 Anomalous photovoltage in BaTiO₃ *Ferroelectrics* **13** 305–7
- [17] Grinberg I et al 2013 Perovskite oxides for visible-light-absorbing ferroelectric and photovoltaic materials *Nature* **503** 509–12
- [18] Hipolito F, Pedersen T G and Pereira V M 2016 Nonlinear photocurrents in two-dimensional systems based on graphene and boron nitride *Phys. Rev. B* **94** 045434
- [19] Peters E C, Lee E J H, Burghard M and Kern K 2010 Gate dependent photocurrents at a graphene p–n junction *Appl. Phys. Lett.* **97** 193102
- [20] Lemme M C, Koppens F H L, Falk A L, Rudner M S, Park H, Levitov S L and Marcus C M 2011 Gate-activated photoresponse in a graphene p–n junction *Nano Lett.* **11** 4134–7
- [21] Gabor N M, Song J C W, Ma Q, Nair N L, Taychatanapat T, Watanabe K, Taniguchi T, Levitov L S and Jarillo-Herrero P 2011 Hot carrier-assisted intrinsic photoresponse in graphene *Science* **334** 648–52
- [22] Yan J, Kim M-H, Elle J A, Sushkov A B, Jenkins G S, Milchberg H M, Fuhrer M S and Drew H D 2012 Dual-gated bilayer graphene hot-electron bolometer *Nat. Nanotechnol.* **7** 472–8
- [23] Freitag M, Low T, Xia F and Avouris P 2013 Photoconductivity of biased graphene *Nat. Photon.* **7** 53–59
- [24] Buscema M, Barkelid M, Zwiller V, van der Zant H S J, Steele G A and Castellanos-Gomez A 2013 Large and tunable photothermoelectric effect in single-layer MoS₂ *Nano Lett.* **13** 358–63
- [25] Echtermeyer J T et al 2014 Photothermoelectric and photoelectric contributions to light detection in metal-graphene-metal photodetectors *Nano Lett.* **14** 3733–42
- [26] Min H, Sahu B, Banerjee S K and MacDonald A H 2007 *Ab initio* theory of gate induced gaps in graphene bilayers *Phys. Rev. B* **75** 155115
- [27] Kuzmenko A B, Crassee I and van der Marel D 2009 Determination of the gate-tunable band gap and tight-binding parameters in bilayer graphene *Phys. Rev. B* **80** 165406
- [28] Malard L M, Nilsson J, Elias D C, Brant J C, Plentz F, Alves E S, Neto A H C and Pimenta M A 2007 Probing the electronic structure of bilayer graphene by Raman scattering *Phys. Rev. B* **76** 201401(R)
- [29] Dresselhaus M S and Dresselhaus G 2002 Intercalation compounds of graphite *Adv. Phys.* **51** 1–186
- [30] Alden J S, Tsen A W, Huang P Y, Hovden R, Brown L, Park J, Muller D A and McEuen P L 2013 Strain solitons and topological defects in bilayer graphene *Proc. Natl Acad. Sci. USA* **110** 11256–60
- [31] McCann E and Koshino M 2013 The electronic properties of bilayer graphene *Rep. Prog. Phys.* **76** 056503
- [32] Zhang F, MacDonald A H and Mele E J 2013 Valley Chern numbers and boundary modes in gapped bilayer graphene *Proc. Natl Acad. Sci. USA* **110** 10546–51
- [33] Kośmider K and Fernández-Rossier J 2013 Electronic properties of the MoS₂-WS₂ heterojunction *Phys. Rev. B* **87** 075451
- [34] Terrones H, López-Urías F and Terrones M 2013 Novel hetero-layered materials with tunable direct band gaps by sandwiching different metal disulfides and diselenides *Sci. Rep.* **3** 1549
- [35] Komsa H-P and Krasheninnikov A V 2013 Electronic structures and optical properties of realistic transition metal dichalcogenide heterostructures from first principles *Phys. Rev. B* **88** 085318
- [36] Chiu M-H et al 2015 Determination of band alignment in the single-layer MoS₂/WSe₂ heterojunction *Nat. Commun.* **6** 7666
- [37] Hill H M, Rigosi A F, Rim K T, Flynn G W and Heinz T F 2016 Band alignment in MoS₂/WS₂ transition metal dichalcogenide heterostructures probed by scanning tunneling microscopy and spectroscopy *Nano Lett.* **16** 4831–7
- [38] Wilson N R et al 2017 Determination of band offsets, hybridization and exciton binding in 2D semiconductor heterostructures *Sci. Adv.* **3** e1601832

- [39] Morimoto T and Nagaoso N 2016 Topological nature of nonlinear optical effects in solids *Sci. Adv.* **2** e1501524
- [40] See supplementary information for a discussion of the configuration dependence of shift vector in vdW materials and homostructures, strained shift current, Hamiltonian of Bernal stacked BLG, and numerical calculation of shift vector for other polarizations
- [41] Mañes J L, Guinea F and Vozmediano M A H 2007 Existence and topological stability of Fermi points in multilayered graphene *Phys. Rev. B* **75** 155424
- [42] Latil S and Henrard L 2006 Charge carriers in few-layer graphene films *Phys. Rev. Lett.* **97** 036803
- [43] Koshino M and McCann E 2010 Parity and valley degeneracy in multilayer graphene *Phys. Rev. B* **81** 115315
- [44] We note that for a spinless system that possesses time-reversal symmetry, the shift vector obeys $\mathbf{r}^{(\eta)}(\Delta, \theta, \mathbf{k}) = \mathbf{r}^{(\eta)}(\Delta, \theta, -\mathbf{k})$. See also full discussion in **SI**
- [45] McCann E and Fal'ko V I 2006 Landau-level degeneracy and quantum Hall effect in a graphite bilayer *Phys. Rev. Lett.* **96** 086805
- [46] Lee C, Wei X, Kysar J W and Hone J 2008 Measurement of the elastic properties and intrinsic strength of monolayer graphene *Science* **321** 385–8
- [47] Kim K S *et al* 2009 Large-scale pattern growth of graphene films for stretchable transparent electrodes *Nature* **457** 706–10
- [48] Bertolazzi S, Brivio J, Stretching K A and 2011 Breaking of ultrathin MoS₂ *ACS Nano* **5** 9703–9
- [49] Conley H J, Wang B, Ziegler J I, Haglund R F, Pantelides S T and Bolotin K I 2013 Bandgap engineering of strained monolayer and bilayer MoS₂ *Nano Lett.* **13** 3626–30
- [50] Yoo H *et al* 2019 Atomic and electronic reconstruction at the van der Waals interface in twisted bilayer graphene *Nat. Mater.* **18** 448–53
- [51] Yang M-M, Kim D J and Alexe M 2018 Flexo-photovoltaic effect *Science* **360** 904–7
- [52] Nadupalli S, Kreisel J and Granzow T 2019 Increasing bulk photovoltaic current by strain tuning *Sci. Adv.* **5** eaau9199
- [53] Kaner N T *et al* 2020 Enhanced shift currents in monolayer 2D GeS and SnS by strain-induced band gap engineering *ACS Omega* **5** 17207
- [54] Zhang W *et al* 2015 Piezostain-enhanced photovoltaic effects in BiFeO₃/La_{0.7}Sr_{0.3}MnO₃/PMN-PT heterostructures *Nano Energy* **18** 315–24
- [55] Lin P, Zhu L, Li D, Xu L, Pan C and Piezo-Phototronic W Z 2018 Effect for enhanced flexible MoS₂/WSe₂ van der Waals photodiodes *Adv. Funct. Mater.* **28** 1802849
- [56] Schankler A M, Gao L, Rappe A M 2020 Large bulk piezophotovoltaic effect of monolayer transition metal dichalcogenides (arXiv:2009.11980 [cond- mat.mes-hall])
- [57] Mucha-Kruczyński M, Aleiner I L and Fal'ko V I 2011 Strained bilayer graphene: band structure topology and Landau level spectrum *Phys. Rev. B* **84** 041404(R)
- [58] Mouldale C, Knothe A and Fal'ko V I 2020 Engineering of the topological magnetic moment of electrons in bilayer graphene using strain and electrical bias *Phys. Rev. B* **101** 085118
- [59] Woessner A *et al* 2016 Near-field photocurrent nanoscopy on bare and encapsulated graphene *Nat. Commun.* **7** 10783
- [60] Sunku S S *et al* 2020 Nano-photocurrent mapping of local electronic structure in twisted bilayer graphene *Nano Lett.* **20** 2958–64
- [61] Sunku S S *et al* 2018 Photonic crystals for nano-light in moiré graphene superlattices *Science* **362** 1153–6
- [62] Alden J S, Tsen A W, Huang P Y, Hovden R, Brown L, Park J, Muller D A and McEuen P L 2013 Strain solitons and topological defects in bilayer graphene *Proc. Natl Acad. Sci. USA* **110** 11256–60